Climate Variability Inferred from a Continuously Stratified Model of the Ideal-Fluid Thermocline*

RUI XIN HUANG

Department of Physical Oceanography, Woods Hole Oceanographic Institution, Woods Hole, Massachusetts

(Manuscript received 9 November 1998, in final form 11 August 1999)

ABSTRACT

Climate variability in the subtropical gyre interior induced by anomalous surface thermal forcing, Ekman pumping, mixed layer depth variability, and anomalous subpolar water formation is examined, using a continuously stratified model of the ideal-fluid thermocline. Cooling (heating) induces a negative (positive) potential vorticity perturbation in the ventilated thermocline, and the associated density perturbations propagate downstream in the form of second and higher baroclinic modes. The second baroclinic mode resembles the traditional second baroclinic mode because it has a thermal structure with cooling (warming) in the upper thermocline and warming (cooling) in the lower thermocline.

Anomalous Ekman pumping can also induce density perturbations that propagate westward in the form of the first baroclinic mode. In addition, if the outcrop lines are nonzonal, there are density perturbations that propagate downstream in the form of the second or third baroclinic modes. Perturbations in the sea surface elevation are mostly confined to the region of anomalous forcing. On the other hand, when the low potential vorticity anomaly in the subpolar mode water spreads into the subtropical basin, both the unventilated and ventilated thermocline move downward. Consequently, temperature at a given depth seems to increase.

1. Introduction

Studying the elementary processes involved in climate anomalies in the ocean's interior is a key step in understanding climate change. In the equatorial ocean, climate variability can be described in terms of linear waves to a very good approximation. For example, the response of an equatorial ocean with continuous stratification to wind stress anomaly can be described in this manner (i.e., Cane and Sarachik 1976; McCreary 1985). In fact, the dynamics of the equatorial wave guide has been used successfully to interpret the climate anomaly related to the El Niño–Southern Oscillation.

On the other hand, our understanding of climate variability for the middle latitude ocean remains rudimentary. Recently, climate anomaly in the middle latitude ocean has been examined through data analysis (e.g., Deser et al. 1996; Joyce et al. 1999; Schneider et al. 1999; Tourre et al. 1999; Zhang 1998; Zhang et al. 1998). The structure of climate variability in the middle latitude ocean has also been analyzed by using simple models (e.g., Huang and Pedlosky 1999; Liu 1999). The analytical studies were based on multilayer models of the ventilated thermocline. In order to understand the complicated nature of climate variability, it is important to examine the climate variability in a more realistic model with continuous stratification that includes the ventilated and unventilated thermocline, and the mixed layer. Thus, our goal in this study is to explore the structure of climate variability in the middle latitude ocean induced by localized anomalous surface forcing and the anomaly in the potential vorticity of the unventilated thermocline.

We use here a continuously stratified model of the ideal-fluid thermocline, forced by idealized surface boundary conditions, including the Ekman pumping and the mixed layer density and depth. The same method used by Huang and Pedlosky (1999) is used in this study, that is, in order to avoid the complication due to wave processes we defined the climate variability as the difference between two steady-state solutions obtained under slightly different forcing. The model formulation is briefly discussed in section 2. In section 3, climate variability induced by anomalous cooling and Ekman pumping is examined by subtracting two solutions obtained under the standard and the anomalous forcing. In addition, we studied the climate variability in the subtropical basin interior induced by anomalous deep-

---

* Woods Hole Oceanographic Institution Contribution Number 9885.

Corresponding author address: Rui Xin Huang, Department of Physical Oceanography, Woods Hole Oceanographic Institution, Woods Hole, MA 02543.
E-mail: rhuang@whoi.edu

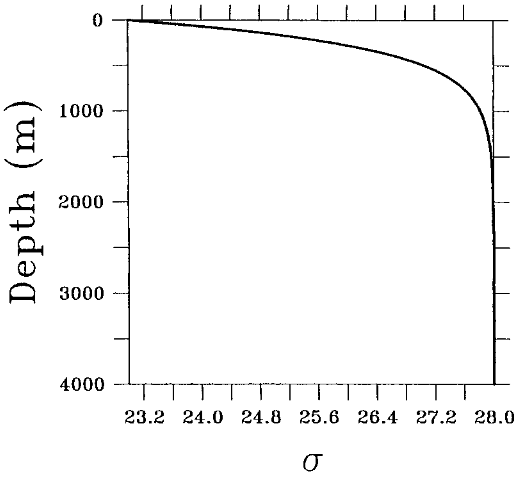

FIG. 1. Background stratification.

water formation in the subpolar basin. Conclusions are drawn in section 4.

2. Model formulation

The model used in this study is adapted from Huang and Russell (1994), and a concise description is also included in Huang (2000). The structure of the thermocline is reduced to solving a second-order ordinary differential equation in density coordinates:

$$B_{\rho\rho} = \frac{fg}{Q(B, \rho)}, \qquad (1)$$

where $Q(B, \rho)$ is the potential vorticity function. For the unventilated thermocline, $Q = f_0\rho_z$, where f_0 is the Coriolis parameter at the northern boundary of the subtropical gyre and ρ_z is the given background stratification. For water below the base of the wind-driven gyre, $Q^a = f\rho_z$, hereafter the superscript a depicts the abyssal water. This equation is subject to constraints

$$B_\rho = -gh(x, y) \qquad \text{at } \rho = \rho^s(x, y); \qquad (2)$$

$$B = B^a(\rho), \qquad B_\rho = B^a_\rho(\rho) \quad \text{at } \rho = \rho^b$$

$$(\rho^b \text{ is unknown}); \qquad (3)$$

$$-\int_{\rho^s}^{\rho^b} B_\rho^2 \, d\rho + \int_{\rho^{se}}^{\rho^b} B_\rho^{a2} \, d\rho = \frac{2g\overline{\rho}f^2}{\beta} \int_x^{x^e} w_e \, dx. \qquad (4)$$

The subtropical basin interior, excluding the western boundary region, is divided into $M \times N$ stations, where M is the number of the outcrop lines and N is the number of stations along each outcrop line. The solution is calculated by solving the above free boundary value problem station by station. For details of such a calculation see Huang (1988) and Huang and Russell (1994).

The model ocean is a rectangular basin of 60° × 30° (from 15°N to 45°N), mimicking the subtropical North Atlantic. The input data required for the calculation include the Ekman pumping rate, the mixed layer density and depth distribution, and the background stratification. In order to study the climate variability, we define a mean climate state, which is controlled by the following mean forcing fields.

The Ekman pumping rate is

$$w_e = -1.0 \times 10^{-4} \sin\left(\pi \frac{y - y_s}{\Delta y}\right), \qquad (5)$$

where $y_s = 15°\text{N}$ is the southern boundary and $\Delta y = 30°$ is the meridional range of the model basin. The background stratification is calculated by assuming a simple advection–diffusion balance

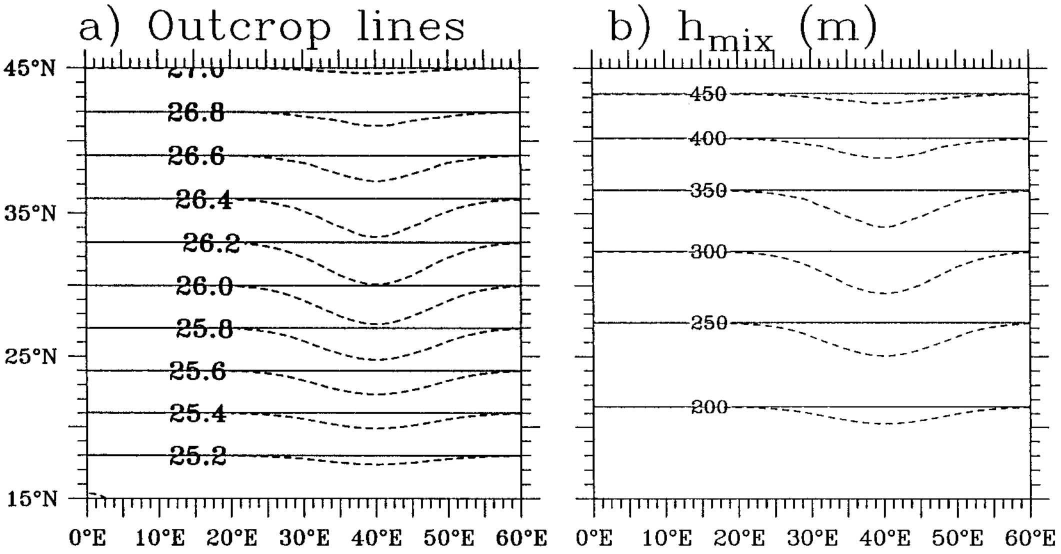

FIG. 2. Surface density distribution in sigma unit (a) and mixed layer depth in meters (b), with the solid lines indicating the standard case and the dashed lines for the case with cooling in the eastern basin.

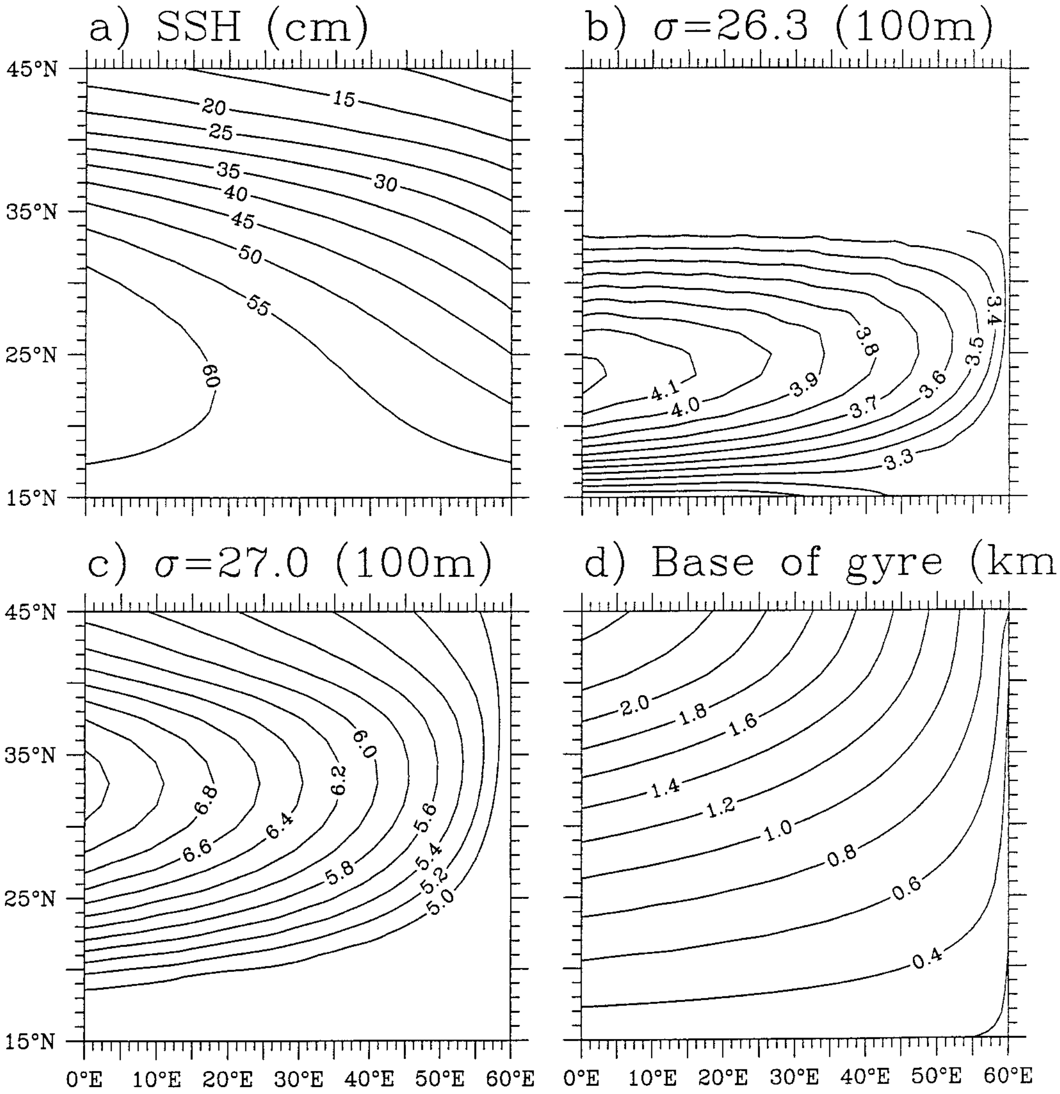

FIG. 3. Mean circulation fields: (a) Sea surface elevation (in cm) (b) depth of isopycnal surface $\sigma = 26.3$ (in 100 m); (c) depth of isopycnal surface $\sigma = 27.0$ (in 100 m); and (d) depth of the base of the wind-driven gyre (in km).

$$w\rho_z = \kappa\rho_{zz}, \tag{6}$$

where $w = 1.0 \times 10^{-5}$ cm s^{-1} is the upwelling velocity, and $\kappa = 0.3$ cm^2 s^{-1} is the vertical diffusivity. The stratification obtained, shown in Fig. 1, is used for the potential vorticity function for the unventilated thermocline. In addition, this profile will also be used as the resting level along the eastern boundary for isopycnals within the mixed layer.

3. Climate variability

In general, climate variability is likely to appear in the form of internal baroclinic modes. Taking the perturbation of (4)

$$\begin{aligned}&-\left(B_\rho^2|_{\rho^b}\delta\rho^b - B_\rho^2|_{\rho^s}\delta\rho^s + 2\int_{\rho^s}^{\rho^b} B_\rho \delta B_\rho\, d\rho\right)\\ &\quad + \left(B_\rho^{a^2}|_{\rho^b}\delta\rho^b - B_\rho^{a^2}|_{\rho^s}\delta\rho^s + 2\int_{\rho^s}^{\rho^b} B_\rho^a \delta B_\rho^a\, d\rho\right)\\ &\quad = \frac{2g\overline{\rho}f^2}{\beta}\int_x^{x^e} \delta w_e\, dx.\end{aligned} \tag{7}$$

Since $B_\rho = B_\rho^a$ at ρ^b, the terms associated with $\delta\rho^b$ cancel. The terms associate with $\delta\rho^s$ also drop out because either $\delta\rho^s$ is zero away from the cooling anomaly or if in the model's formulation mixed layer depth is the same as the reference depth from the background

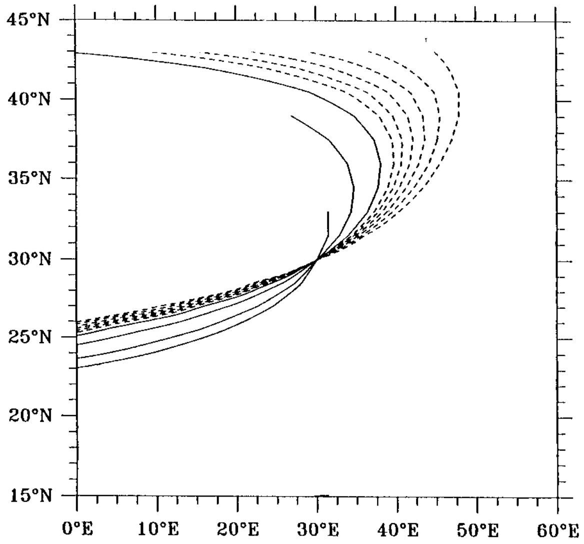

FIG. 4. Streamlines (characteristics) passing through a station in the middle of the model basin. The solid lines indicate the streamlines in the ventilated thermocline, and the dashed lines indicate the streamlines in the unventilated thermocline.

stratification (this is the choice made in this study.) Thus,

$$-\int_{\rho^s}^{\rho^b} B_\rho \delta B_\rho \, d\rho + \int_{\rho^s}^{\rho^b} B_\rho^a \delta B_\rho^a \, d\rho = \frac{g\overline{\rho} f^2}{\beta} \int_x^{x^e} \delta w_e \, dx. \tag{8}$$

First, we assume that both the background stratification and the Ekman pumping are unchanged. Noting that $B_\rho = gz$, we obtain

$$\int_{\rho^s}^{\rho^b} z\delta z \, d\rho = 0. \tag{9}$$

Therefore, the depth perturbation must be in the form of internal modes, with a depth-weighted zero mean. Depth perturbation is, thus, large in the upper thermocline, but small in the low thermocline.

Second, we will study a case in which the potential vorticity of the unventilated thermocline is reduced. Specifically, we will assume that isopycnal surfaces in the low thermocline move downward, so $\delta B_\rho^a = g\delta z(\rho) < 0$ and (8) leads to

$$\int_{\rho^s}^{\rho^b} B_\rho \delta B_\rho \, d\rho = \int_{\rho^s}^{\rho^b} B_\rho^a \delta B_\rho^a \, d\rho > 0. \tag{10}$$

According to this relation, the vertical displacement of isopycnal surfaces should all move downward, although high internal modes can exist at the same time.

Third, when the Ekman pumping is intensified alone, the response of the system can be examined using the following relation

$$\int_{\rho^s}^{\rho^b} B_\rho \delta B_\rho \, d\rho = -\frac{g\overline{\rho} f^2}{\beta} \int_x^{x^e} \delta w_e \, dx. \tag{11}$$

According to this relation, stronger Ekman pumping should induce a downward movement of all isopycnals in the thermocline. Since perturbations are limited to the base of the wind-driven gyre, these perturbations should have a strong projection onto the first baroclinic mode, although high internal modes may exist too.

a. Climate variability due to cooling

As the first example, we examine the climate variability induced by cooling the surface mixed layer within a patch in the eastern basin:

$$\Delta\rho = -0.2 \exp\left[-\frac{(y - y_0)^2 + (x - x_0)^2}{(\Delta x)^2}\right], \tag{12}$$

where $x_0 = 40°\text{E}$, $y_0 = 30°$, and $\Delta x = 10°$. We have made another assumption that the mixed layer depth remain the same along the same isopycnal outcrop line. The effect of changing the mixed layer depth alone is similar and will be discussed shortly. The unperturbed and perturbed mixed layer density and depth distribution are shown in Fig. 2. The wind-driven circulations under these two sets of forcing fields were calculated, and the difference between these two solutions is the climate variability we want to learn about.

Under the undisturbed forcing there is a well-defined anticyclonic gyre in the subtropical basin, as displayed in Fig. 3, including the sea surface elevation (inferred from the Bernoulli function distribution in the mixed layer), the depth of isopycnal surface $\sigma = 26.3$ and 27.0 (this is the isopycnal that outcrops along the northern boundary of the subtropical basin), and the base of the wind-driven gyre.

As discussed by Huang and Pedlosky (1999), perturbations due to changes in the forcing boundary conditions propagate downstream along characteristics, which is defined by streamlines in each individual layer. For a continuously stratified model, it can be shown that streamlines are simple characteristics; see the appendix. Thus, the domain of dependence for a given station is determined by tracing upstream along streamlines passing through this station. Similarly, the domain of influence for a given station is determined by tracing downstream along streamlines passing through this station (Fig. 4). The spiral nature of streamlines passing through a given station is due to the well-known beta spiral discussed in many studies. Note that streamlines in the ventilated thermocline stop at the latitudes where the corresponding isopycnal outcrops.

Furthermore, the perturbation created on a given isopycnal surface at a station may create perturbations in isopycnals shallower that the original one. As a result, perturbations may spread slightly wider than the characteristic cone defined above, and this will be discussed shortly.

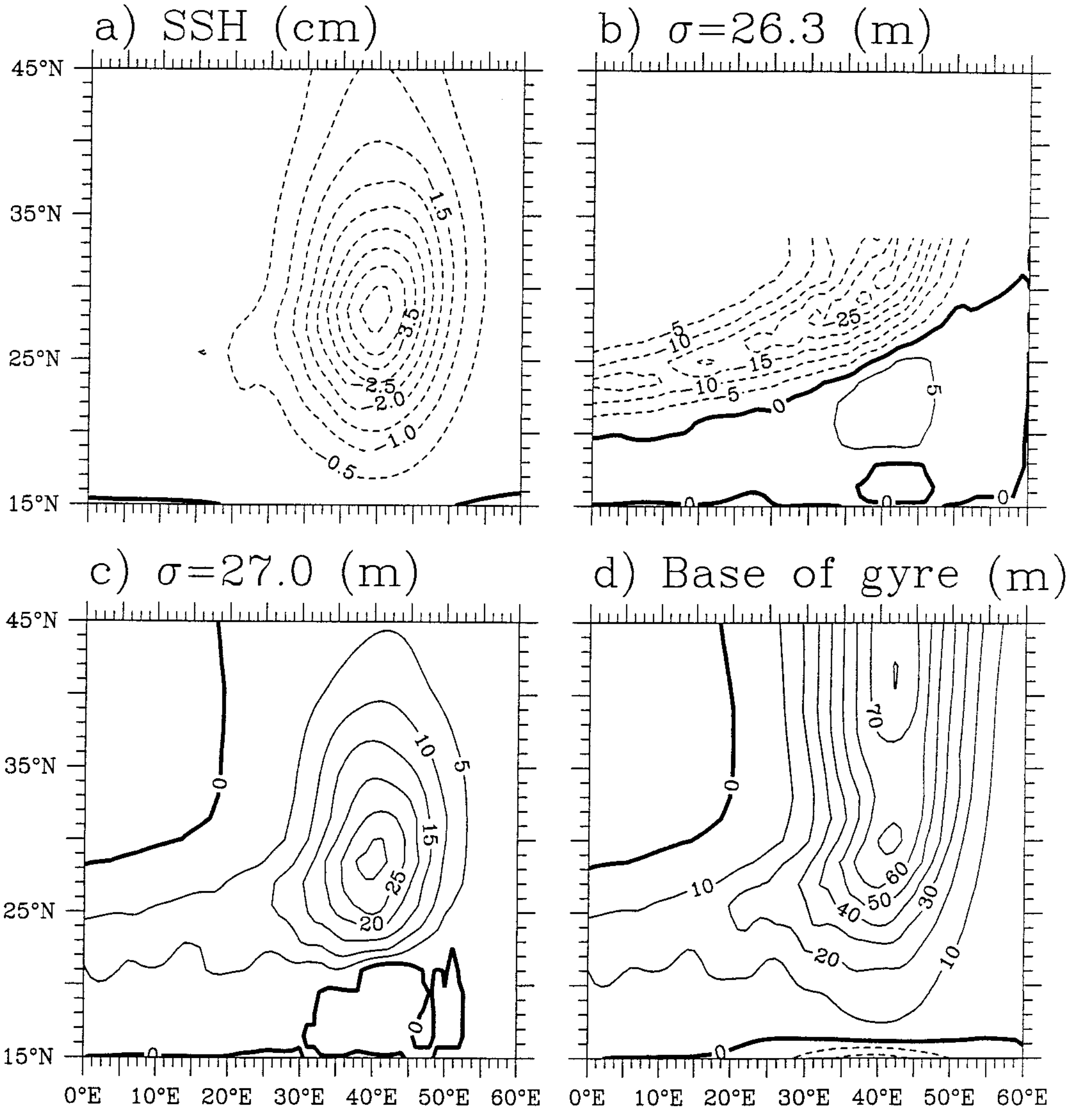

FIG. 5. Perturbation of the mean fields under a localized cooling: (a) Sea surface elevation (in cm); (b) depth of isopycnal surface σ = 26.3 (in m); (c) depth of isopycnal surface σ = 27.0 (in m); and (d) depth of the base of the wind-driven gyre (in m).

Under the localized cooling the free surface elevation declines and reaches a minimum of −5 cm at the center of the cooling patch (Fig. 5a). The shallow isopycnal surfaces all move upward and the layer thickness perturbation is confined within the characteristic cone originating from the cooling region. For example, isopycnal surface σ = 26.3 moves upward with a maximum displacement of 30 m; see Fig. 5b. On the other hand, deeper isopycnal surfaces move downward. The isopycnal surface σ = 27.0 moves downward with a maximum of 30 m; see Fig. 5c. The base of wind-driven gyre also moves downward, with a maximum vertical displacement of 70 m. The perturbation patterns presented here are quite consistent with those obtained from the much simpler multilayer model of the ventilated thermocline, as discussed by Huang and Pedlosky (1999). In comparison, isopycnal displacement induced by surface cooling estimated from a simple two-layer ventilated thermocline model may be exaggerated, while the model used in this study may provide better estimate.

The horizontal spreading of the perturbations due to cooling varies, depending on the choice of the physical properties. Although the depth perturbation on isopycnal surface σ = 26.3 gradually declines downstream, it remains rather strong all the way up to the western boundary (Fig. 5b). The σ = 27.0 isopycnal surface is the boundary between the ventilated and unventilated thermocline. The perturbation of the depth of this isopycnal is mostly confined to the source of the cooling. Similarly, the perturbation of the base of the wind-driv-

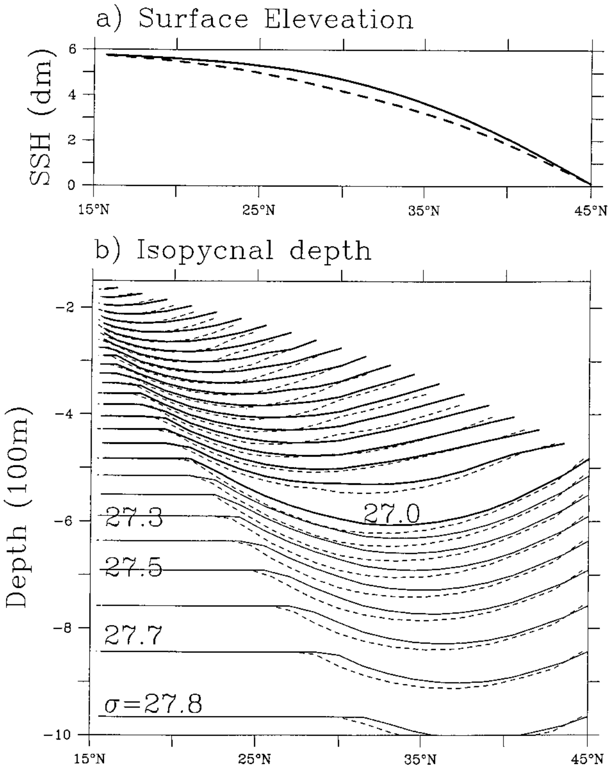

FIG. 6. A meridional section along 40°E. The solid lines for the standard case and the dashed lines for the case with cooling: (a) The sea surface elevation (in decimeters) and (b) the isopycnal surface distribution.

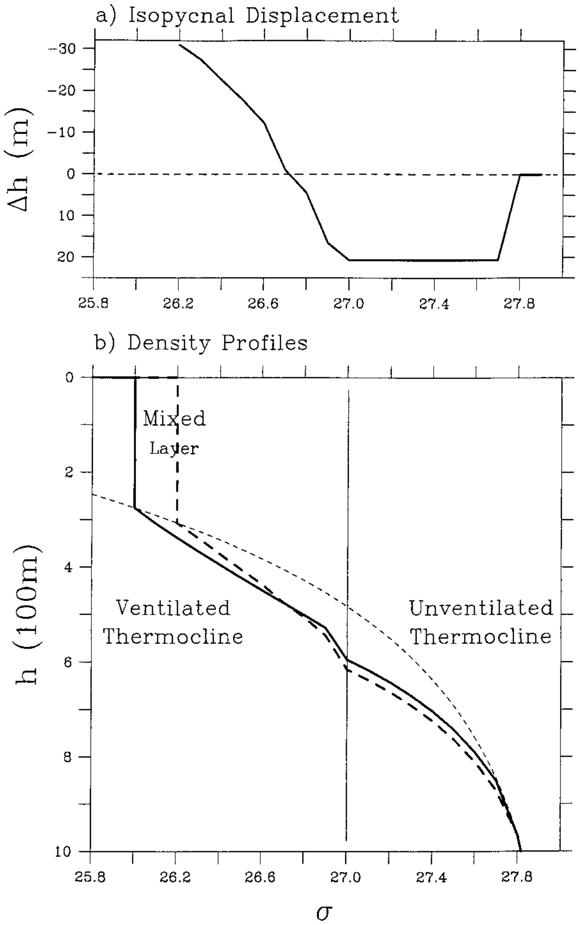

FIG. 7. A density profile at 30°N, 40°E: (a) The vertical displacement of isopycnals due to cooling (in m) and (b) the density profiles, with the solid line for the standard case and the dashed line for the case with cooling. The thin dashed line indicates the background stratification.

en gyre is largely confined to the source of cooling. Although there is a small perturbation that reaches the western boundary as well (Fig. 5c).

On the other hand, the free surface elevation seems to be confined to the region of the cooling anomaly, with virtually no downstream propagation (Fig. 5a). Thus, away from the surface buoyancy forcing anomaly, the perturbations appear primarily in forms of internal modes. It seems that such internal variability may be difficult to be detected by satellite measurements alone. In this regard, this continuous model is distinctly different from the multilayer model discussed by Huang and Pedlosky (1999). It is readily seen that the perturbation in the equivalent free surface elevation in a multilayer model is primarily determined by the upper-layer depth perturbation multiplied by a reduced gravity of the top layer. As a result, the free surface elevation anomaly inferred from such a simple multilayer model would have a strong anomaly propagating downstream within the characteristic cone defined by the streamlines from the outer edge of the cooling region.

The vertical structure of the perturbations can be seen clearly through a vertical section along 40°E (Fig. 6). Cooling leads to a decline of sea surface elevation along this section (Fig. 6a). Most importantly, cooling-induced perturbation is primarily in the form of a second baroclinic mode, that is, the upper part of the thermocline is cooled and the lower part of the thermocline is warmed up (Fig. 6b).

The vertical structure of the perturbation has a very clearly defined second baroclinic mode, as shown in Fig. 7. Since this is due to a finite-amplitude perturbation, the isopycnal displacement does not necessarily satisfy constraint (9) exactly. In the upper part of the thermocline, cooling leads to upward movement of the isopycnal surface, and in the lower part of the thermocline surface cooling leads to a downward movement of the thermocline. This figure can be interpreted in the potential vorticity language. Since Δh (isopycnal depth) monotonically increases downward, the layer thickness perturbation is positive for all ventilated layers. Thus, potential vorticity is reduced due to cooling on the surface layer. The downstream movement of this cooling-induced low potential vorticity anomaly induces the dynamic changes in the circulation seen from these figures.

The surface-cooling-induced low potential vorticity

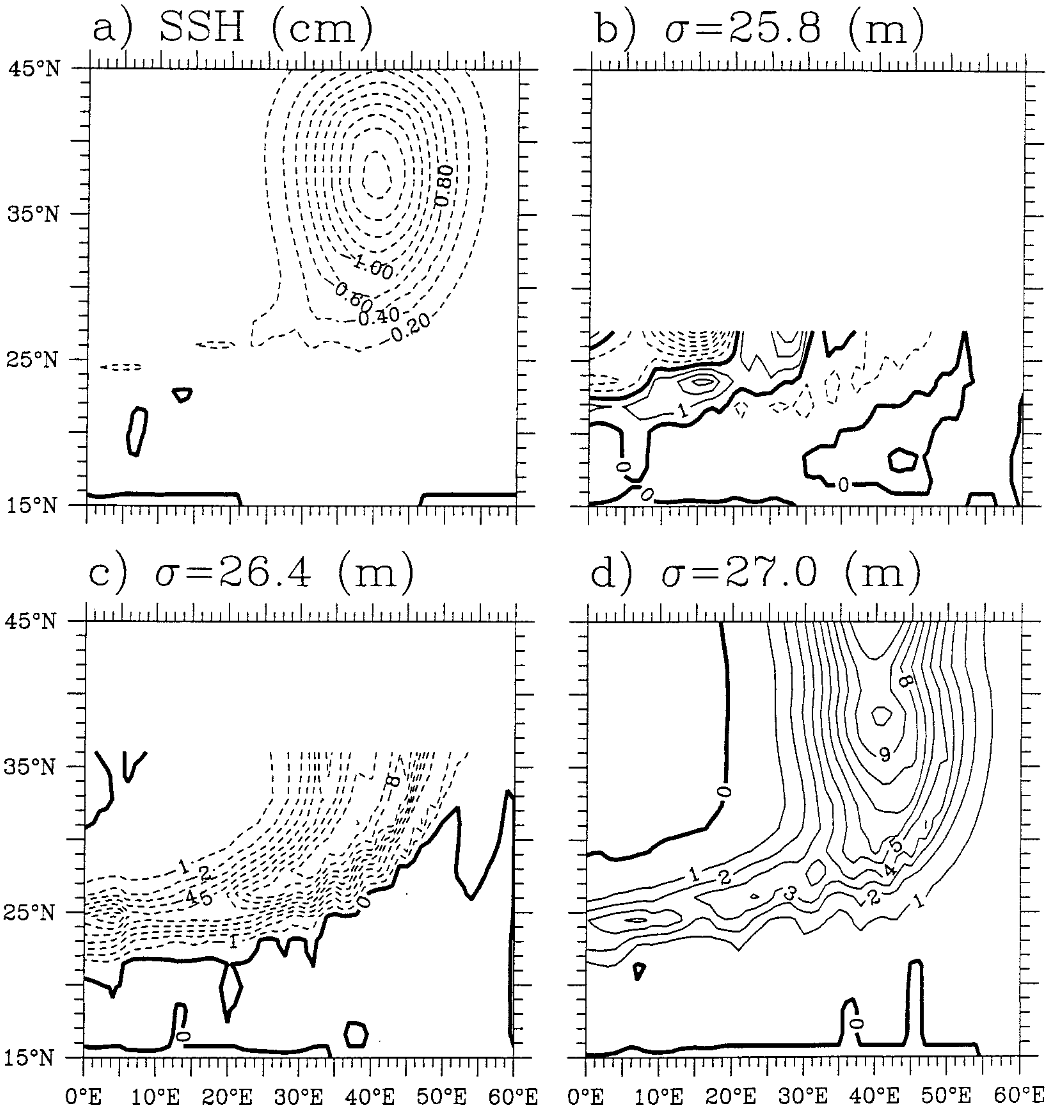

FIG. 8. Perturbation of the mean fields under a localized cooling at 38°N, 40°E: (a) Sea surface elevation (in cm); (b) depth of isopycnal surface σ = 25.8 (in m); (c) depth of isopycnal surface σ = 26.4 (in m); and (d) depth of isopycnal surface σ = 27.0 (in m).

anomaly can be explain in terms of simple kinematics. For simplicity, let us assume a two-dimensional flow. Using the continuity equation, we have

$$\rho_z = -\frac{v}{S_u}\rho_y, \tag{13}$$

where S_u is the subduction rate. This is a simple kinematic statement that horizontal density gradient is purely advected into the ocean interior during the subduction process, and this is the classical picture of water mass formation (e.g., Iselin 1939). Using the linear Sverdrup relation, that is, the linear vorticity balance equation, we have

$$v = \frac{f}{\beta h}w_e, \tag{14}$$

where h is the depth of the wind-driven circulation. For simplicity, we will assume the mixed layer is shallow and flat, so that $S_u \approx w_e$. Under these approximations, we obtain a simple relation between potential vorticity of the subducted water and the meridional density gradient in the mixed layer:

$$q = -f\rho_z = \frac{f^2}{\beta h}\rho_y. \tag{15}$$

When anomalous cooling is applied to a region of the ocean, the meridional density gradient is reduced, so potential vorticity of the subducted water declines.

On the other hand, because the potential thickness of the unventilated thermocline is fixed by the input function of the so-called background stratification along the

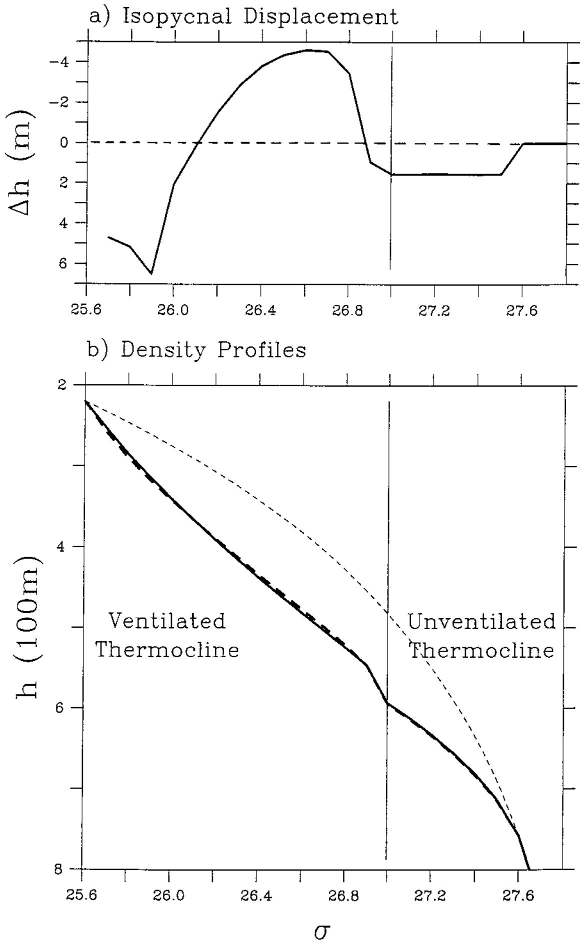

FIG. 9. A density profile at 24°N, 15°E: (a) The vertical displacement or isopycnals due to cooling (in m) and (b) the density profiles, with the solid line for the standard case and the dashed line for the case with cooling. The thin dashed line indicates the background stratification.

intergyre boundary, the downward motion of the unventilated thermocline layers is constant. (The linear segment of the curve in Fig. 7a is for the isopycnal that was under the base of the wind-driven gyre under the unperturbed forcing.) Since the downward migration of the thermocline is equivalent to an increase in temperature at a fixed location, surface cooling induces a warming within the lower part of the thermocline.

Our calculations show that density perturbations due to a localized cooling in the southern half of the basin are primarily in the form of a second baroclinic mode. However, if the cooling source is located in the northern half of the gyre, there is indeed a third baroclinic mode response to the surface cooling. In the following example the cooling source is in the form

$$\delta\rho = -0.08 \exp\left[-\frac{(y - y_0)^2}{(\Delta y)^2} - \frac{(x - x_0)^2}{(\Delta x)^2}\right], \quad (16)$$

where $x_0 = 40°$, $y_0 = 38°$, $\Delta x = 10°$, and $\Delta y = 8°$. Cooling reduces the sea surface elevation. Similar to the previous case, the anomaly in the sea surface elevation is mostly confined to the region of cooling. Below the sea surface, the isopycnal depth perturbations appear in the form of the third baroclinic mode, as seen from Figs. 8b–d. In addition, there are complicated patterns on the shallow isopycnal surfaces, such as the negative–positive–negative bands on $\sigma = 25.8$ (Fig. 8b). Thus, the vertical structure of the perturbations should be a mixture of the second and third baroclinic modes.

The vertical structure of the third baroclinic mode can be seen more clearly through the density profile at a station, say 24°N, 15°E. There is a well-defined third baroclinic mode, that is, warm–cold–warm, in the structure of the density perturbation (Fig. 9). This form of density anomaly is consistent with the density anomaly in the form of the third baroclinic mode discussed by Huang and Pedlosky (1999).

Although our analysis has been focused on the case of a surface density anomaly induced by thermal forcing, the analysis can apply to a climate anomaly due to surface buoyancy flux anomaly in general, including both cooling (heating) or freshening. P. Chang (1998, personal communication) has identified a thermal anomaly in the form of a second mode, that is, cold–warm, from the North Atlantic climate data, and R. Lukas (1998, personal communication) has recently identified a salinity anomaly in the form of a third baroclinic mode, that is, fresh–salty–fresh, from the Hawaii oceanic time series observations.

In the cases discussed above, the thermal anomalies cover a large area of the upper ocean. Although such studies provide insight into the climate variability in the oceans, it is important to study the oceanic response to a single point source of thermal anomaly. Thus, a series of runs have been carried out where the source of thermal anomaly is confined to a single outcrop line. Furthermore, the zonal width of the cooling anomaly is gradually reduced. For the technical reason of numerical convergence, our numerical experiments have been limited to the resolution of 181 grid points in the zonal direction and 20 ventilated layers. In order to maximize the resolution of the model, we put the first outcrop line at 41°N and 19 ventilated layers into the middle latitude (17.5°–31°N—this is the latitude band where the wave patterns are concentrated), with isopycnal interval of 0.05 σ unit.

In the first set of experiments, the model has 121 grid points in the zonal direction, corresponding to a zonal resolution of 0.5°. The surface cooling is located along the first outcrop line (41°N). As the size of the cooling anomaly is reduced to a narrow band with the half width of the Gaussian profile of 4°, the layer depth perturbation appears in form of two strips of opposite signs (Figs. 10a,b). Note that there is no data point between 31° and 41°N. Thus, the depth anomaly near the cooling source seems to cover a large area meridionally, but this is a graphic artifact due to the rather low meridional reso-

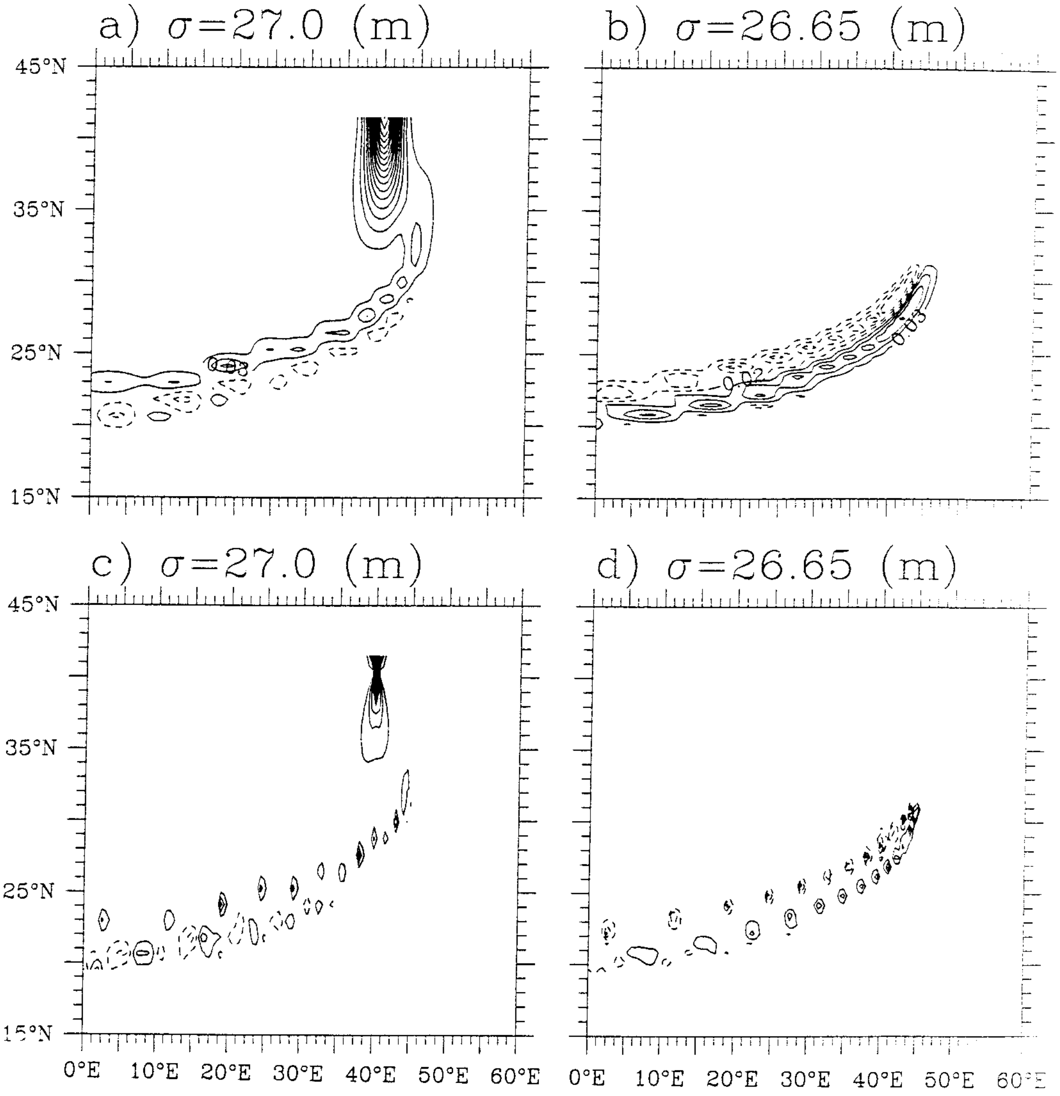

FIG. 10. Perturbation of the mean fields from a model with 121 × 21 grid points and under a localized cooling along a single outcrop line, with $\delta y = -0.05°$ and a width of $\delta x = 4°$ for (a) and (b); $\delta x = 0.2°$ for (c) and (d).

lution in this latitude band. There are also clear signs of small scale (high wavenumber) waves in these patterns. As the width of the cooling band is reduced to 0.2°, corresponding to a point source in this numerical model, the pattern remain basically unchanged.

To test the model's sensitivity to the zonal resolution, we run a model with 181 grid points in the zonal direction, corresponding to a zonal resolution of ⅓°. Again, the patterns of the perturbation induced by the point source do not change (Fig. 11). Our numerical experiments based on the model implies that a point source of the thermal anomaly may produce perturbations that resemble stationary waves. In term of horizontal modes, such wave patterns seem to be a mixture of relatively large amplitude low modes and small amplitude high modes.

In addition, the domain of these waves is confined within a characteristic cone defined as follows. First, the potential vorticity anomaly is carried downstream in the layer, r_1, where it originally formed. Thus, the streamline in this layer defines the western edge of this characteristic cone, as depicted by the solid line CDH in Fig. 12. As this potential vorticity anomaly is carried downstream, crossing the next outcrop line at point D, a new potential vorticity anomaly is created in the layer above, r_2. Since a velocity vector rotates in the beta-spiral sense, the velocity vector in the upper layer r_2 (solid line) is to the right relative to the velocity in the layer below, r_1, (dashed arrows). Similarly, when the potential vorticity perturbation carried by a streamline in layer r_2 meets a new outcrop line at point E, a new potential vorticity anomaly is created in layer r_3, and it move to the right of the streamline in layer r_2. Thus, velocity vectors in the uppermost ventilated layer form

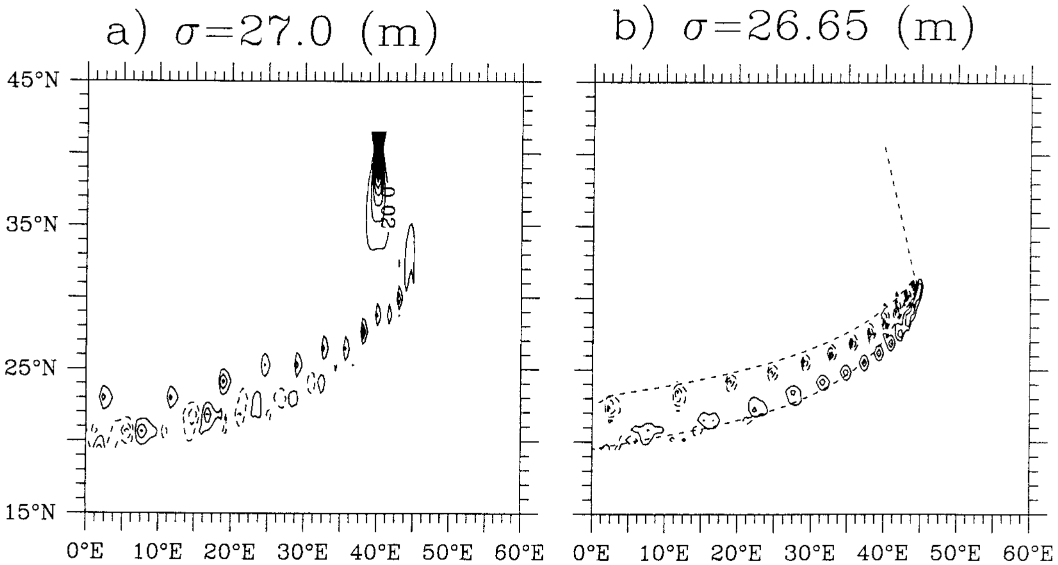

FIG. 11. Perturbation of the mean fields from a model with 181 × 21 grid points and under a localized cooling along a single outcrop line, with $\delta y = -0.05°$ and a width of $\delta x = 0.2°$.

an envelope CDEFG, which works as the eastern edge of the characteristic cone. For example, the thin dashed line in Fig. 11b indicates such a characteristic cone calculated from the solution, and wavelike perturbations induced by the point source are clearly confined within this cone.

In vertical sections, these wavelike patterns also appear in forms of second, third, or higher baroclinic modes (Fig. 13). As discussed above, perturbations induced by a small surface thermal forcing should appear in the form of an internal mode, with a zero depth-weighted mean. Although our numerical results are mostly confined to second and third baroclinic modes, the possibility of higher modes should not be ruled out.

b. Perturbation due to variability in the mixed layer depth

The examples discussed above are limited to the change of mixed layer density, while the mixed layer

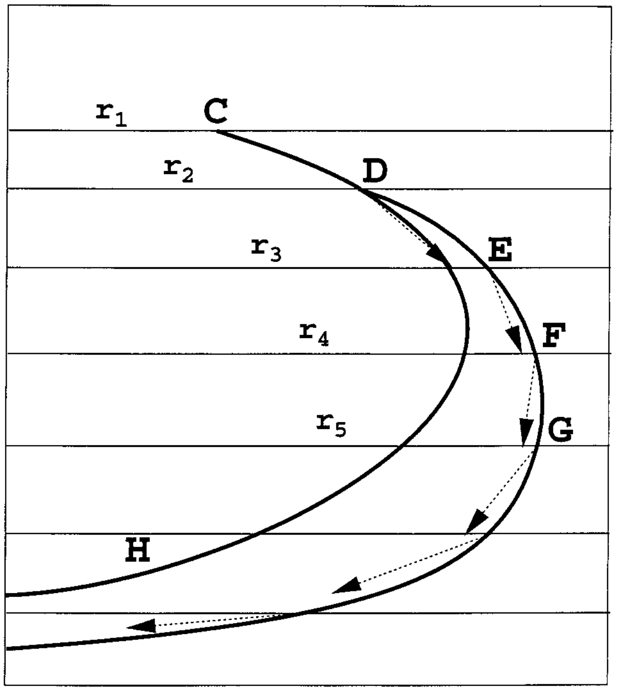

FIG. 12. A schematic diagram for the domain of influence due to a point source C, defined by the envelopes, CDH and CDEFG, of the characteristics stemmed from the source.

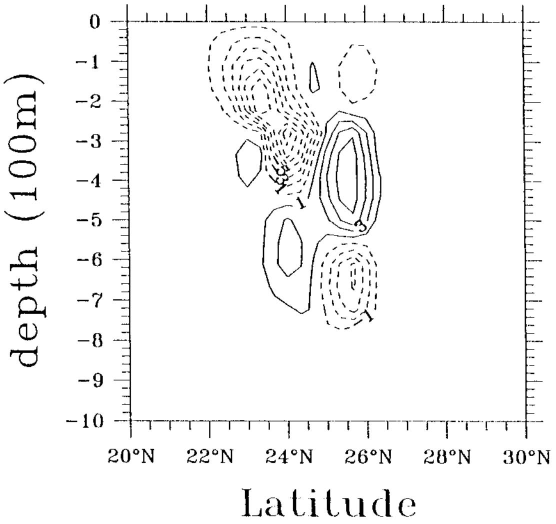

FIG. 13. Depth perturbation (in cm) along 30°E from a model with 181 × 21 grid points under a localized cooling along the first outcrop line ($\sigma = 26.7$) with $\delta y = -0.05°$ and a width of $\delta x = 1°$.

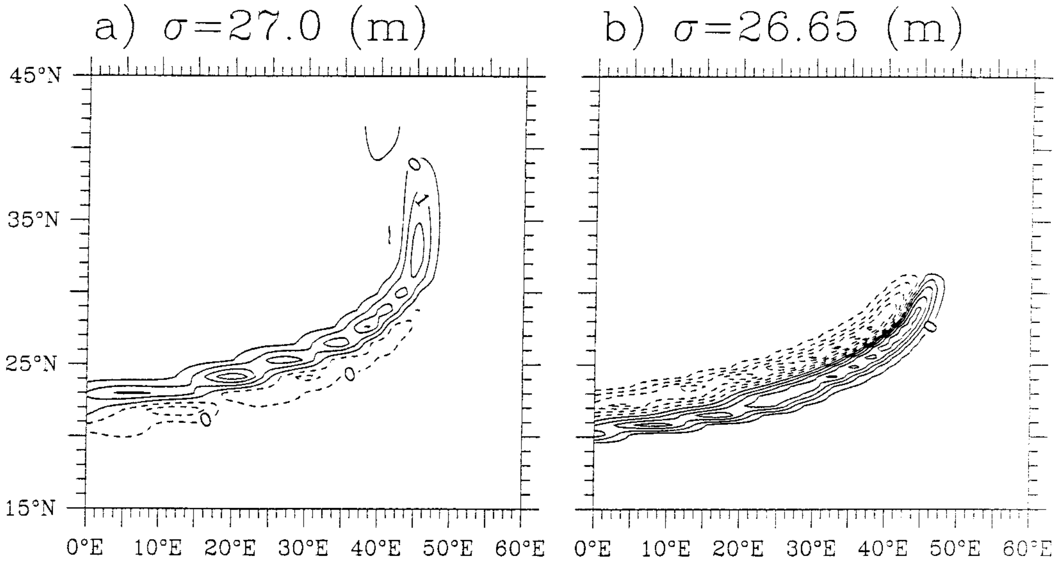

FIG. 14. Perturbation of the mean fields from a model with 181 × 21 grid points and the mixed layer depth 5 m shallower along the first outcrop line ($\sigma = 26.7$) with $\delta y = -0.05°$ and a width of $\delta x = 10°$.

depth is fixed to the value equal to the depth of the corresponding isopycnal surface along the eastern boundary. However, from a physical point of view, mixed layer shoaling (deepening) should create low (high) potential vorticity water in the uppermost ventilated thermocline; thus, mixed layer shoaling is equivalent to cooling. As an example, we show a case where the mixed layer depth along a single outcrop line is reduced 5 m, with a zonal Gaussian profile of 10° wide. The pattern of the layer depth perturbations, shown in Fig. 14, looks quite similar to that due to cooling, shown in Figs. 10a,b.

c. *Climate variability due to anomalous Ekman pumping*

According to our discussion above [i.e., Eq. (11)], the Sverdrup relation implies that changes in the Ekman pumping must induce perturbations that have a strong projection in the first baroclinic mode. In addition, such perturbations should propagate westward from the source of the Ekman pumping anomaly. We have carried out several experiments in which the outcrop lines are all zonal. Indeed, perturbations created by Ekman pumping anomalies have a clearly defined structure in the

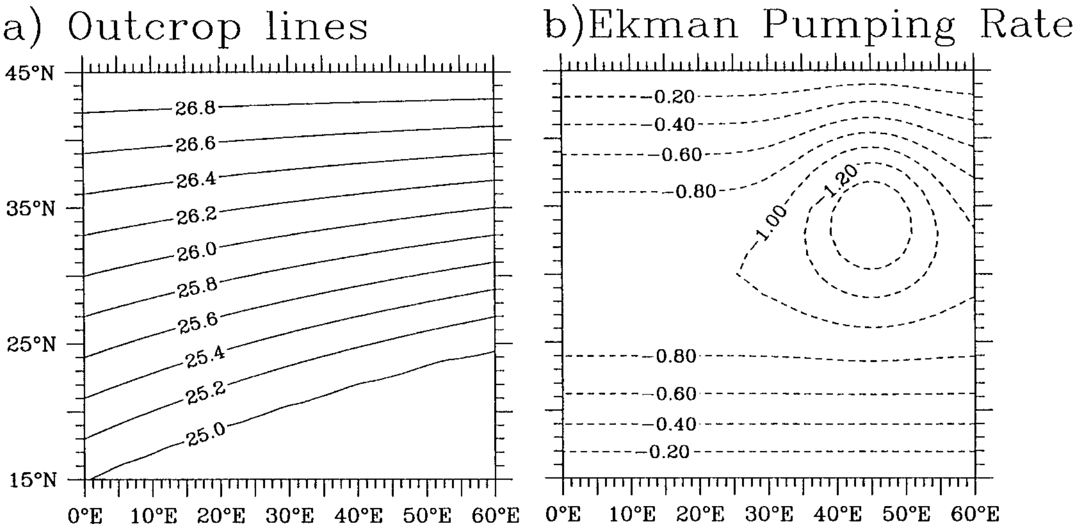

FIG. 15. Mixed layer density distribution for the case of Ekman pumping anomaly (a) and Ekman pumping rate for the case with stronger pumping anomaly, in 10^{-4} cm s^{-1} (b).

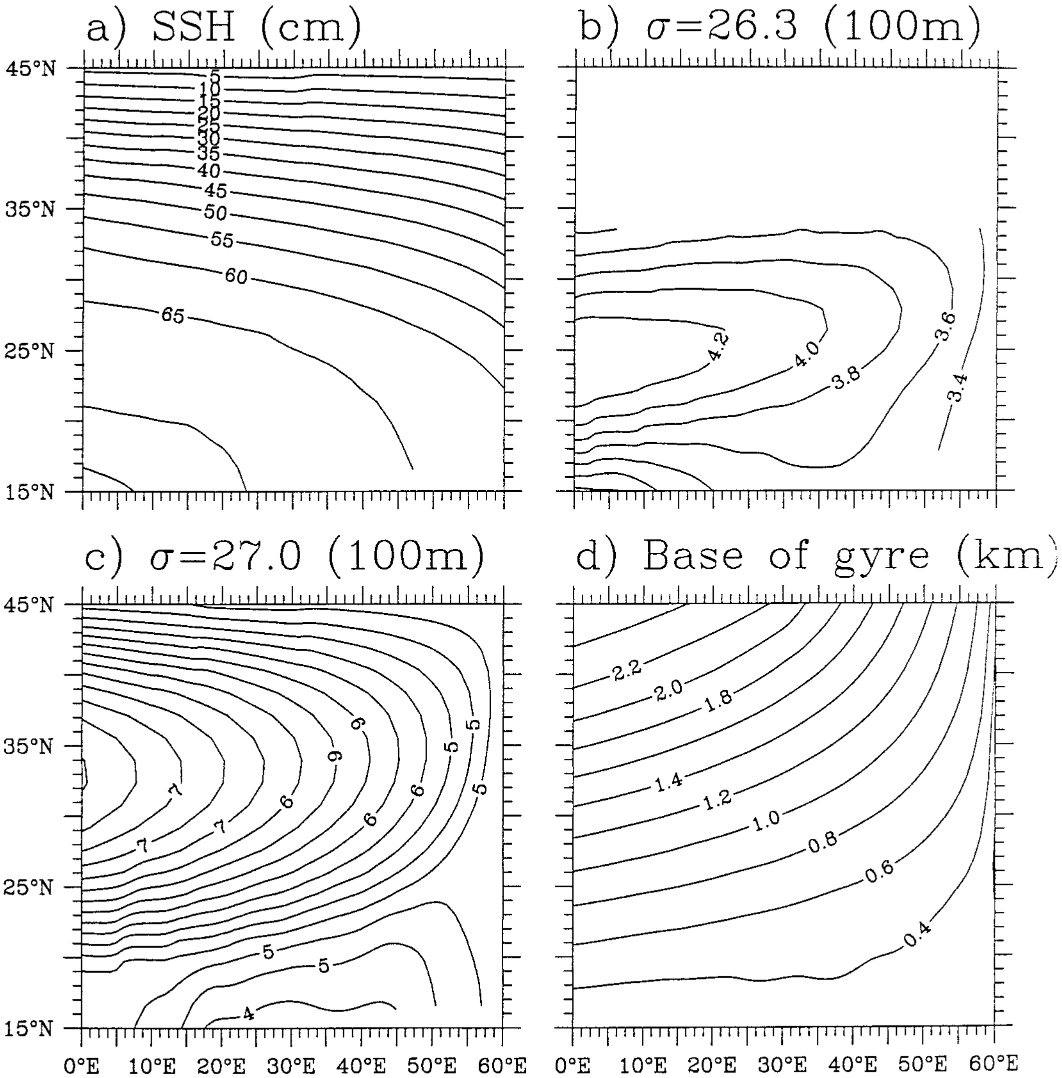

FIG. 16. Mean circulation fields: (a) Sea surface elevation (in cm); (b) depth of isopycnal surface $\sigma = 26.3$ (in 100 m); (c) depth of isopycnal surface $\sigma = 27.0$ (in 100 m); and (d) depth of the base of the wind-driven gyre (in km).

first baroclinic mode. In fact, all isopycnals move downward if the Ekman pumping intensifies. Furthermore, there is no perturbation south of the Ekman pumping anomaly. Since such perturbations are governed by the Sverdrup constraint and their structure is well-known, the results obtained for the cases with zonally oriented outcrop lines are not shown here.

On the other hand, if the outcrop lines are nonzonal, an Ekman pumping anomaly can create perturbations that have complicated structure and propagate southwestward within the characteristic cone, as discussed by Huang and Pedlosky (1999). Here we discuss one example, in which the outcrop lines have a SW–NE orientation (Fig. 15a). The model ocean is driven by a simple sinusoidal Ekman pumping in the unperturbed case. The structure of the circulation driven by such forcing fields is shown in Fig. 16.

We studied the change in the circulation forced by an anomaly in the Ekman pumping rate, as shown in Fig. 15b. Note that the Ekman pumping anomaly has a Gaussian profile

$$\delta w_e = \Delta w_e \exp\left[-\frac{(y - y_0)^2}{(\Delta y)^2} - \frac{(x - x_0)^2}{(\Delta x)^2}\right], \quad (17)$$

where $\Delta w_e = -0.75 \times 10^{-4}$ cm s^{-1}, $x_0 = 40°$, $y_0 = 38°$, $\Delta x = 10°$, $\Delta y = 8°$.

Within the latitudinal band of the Ekman pumping anomaly, the perturbation has a clearly defined structure in the first baroclinic mode, very similar to the case of forcing the model (whose outcrop lines are zonal) with an Ekman pumping anomaly. This component of perturbation propagates westward from the forcing region, as shown in the surface elevation anomaly (Fig. 17a),

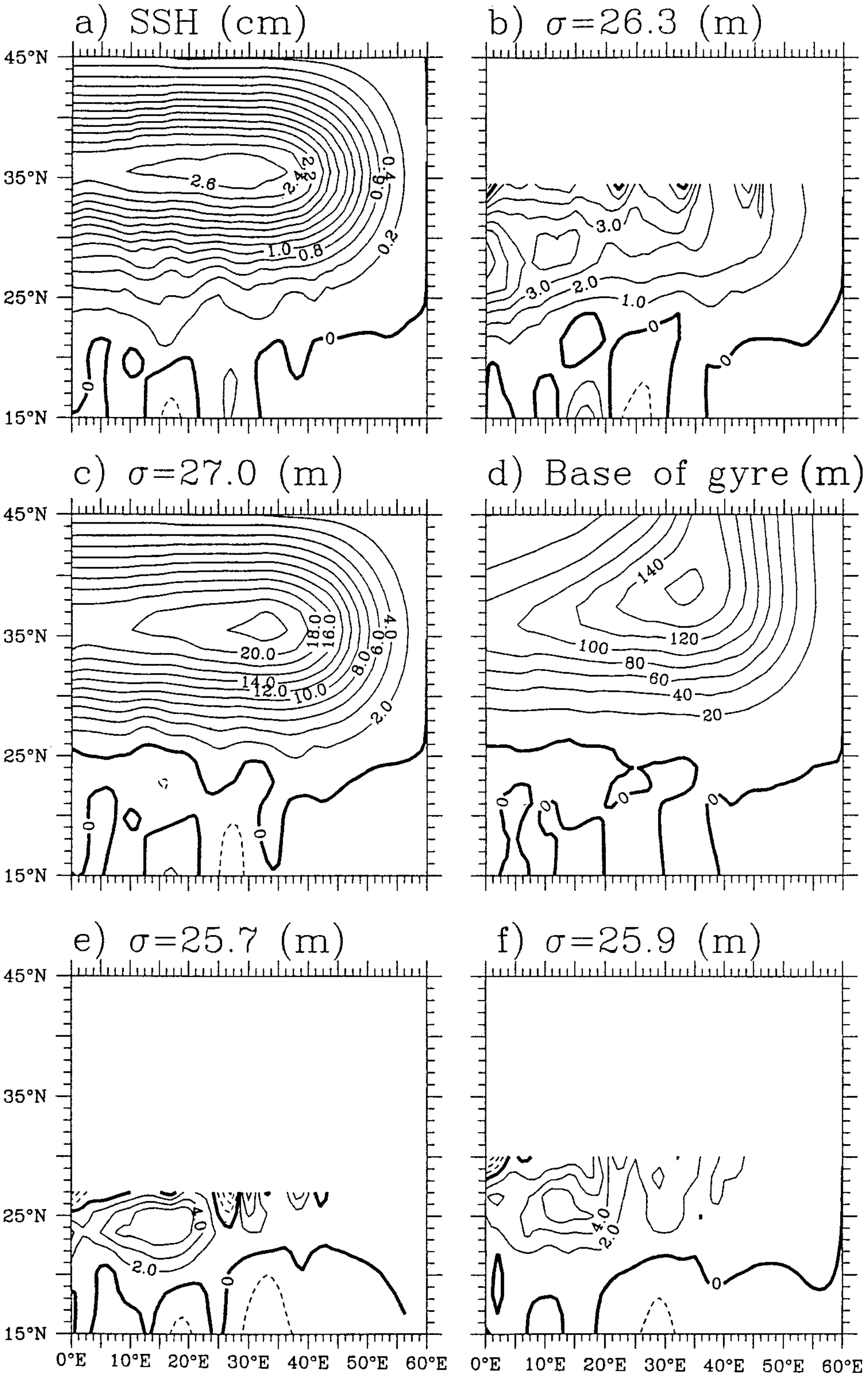

FIG. 17. Perturbation of the mean fields under a stronger Ekman pumping: (a) Sea surface elevation (in cm); (b) depth of isopycnal surface σ = 26.3 (in m); (c) depth of isopycnal surface σ = 27.0 (in m); (d) depth of the base of the wind-driven gyre (in m); (e) depth of isopycnal surface σ = 25.7 (in m); and (f) depth of isopycnal surface σ = 25.9 (in m).

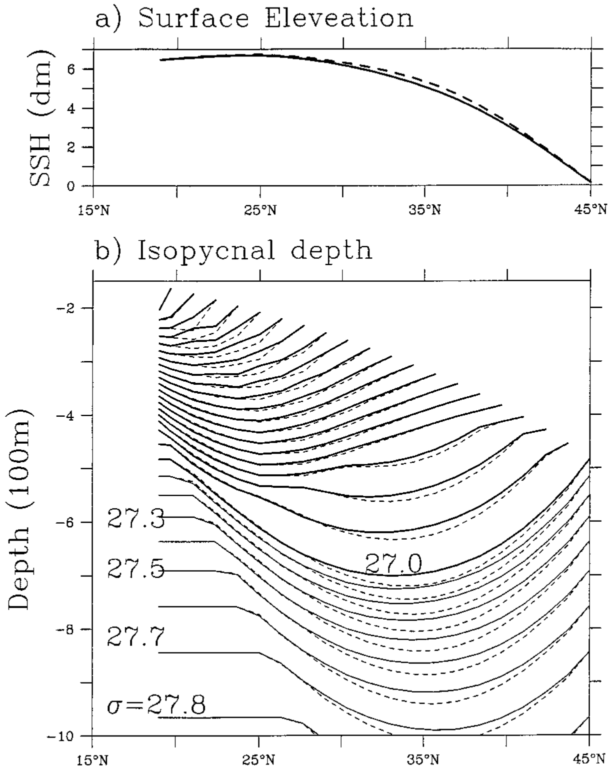

FIG. 18. A meridional section along 20°E solid lines for the standard case and dashed lines for the case with cooling: (a) The sea surface elevation (in decimeters) and (b) the isopycnal surface distribution.

the layer depth anomaly at $\sigma = 27.0$ (Fig. 17c), and the base of wind-driven gyre (Fig. 17d).

Perturbations in the form of the first baroclinic mode is primarily confined north of 25°N, as indicated in these figures. However, on the shallow isopycnal surfaces the perturbations appear near the western boundary south of 25°N, as seen in Figs. 17b,e,f. Thus, perturbations in the form of second or higher modes propagate downstream southwestward.

In order to examine the vertical structure of the perturbation, we plot a meridional section along a section 20° west of the eastern boundary (Fig. 18). Note that in the perturbed solution isopycnals in the region of anomalous forcing move downward; however, in the southern basin, isopycnals in the lower thermocline move upward slightly, indicating the existence of the third baroclinic model; see Figs. 18b and 19. The results obtained from this continuous model are consistent with the results obtained from the two-layer ventilated thermocline model by Huang and Pedlosky (1999).

Note that the anomaly in sea surface elevation is also confined to the region west of the Ekman pumping anomaly and there is virtually no anomalous signal south of the perturbation band. This is similar to the case of the anomaly induced by local cooling discussed in the previous section.

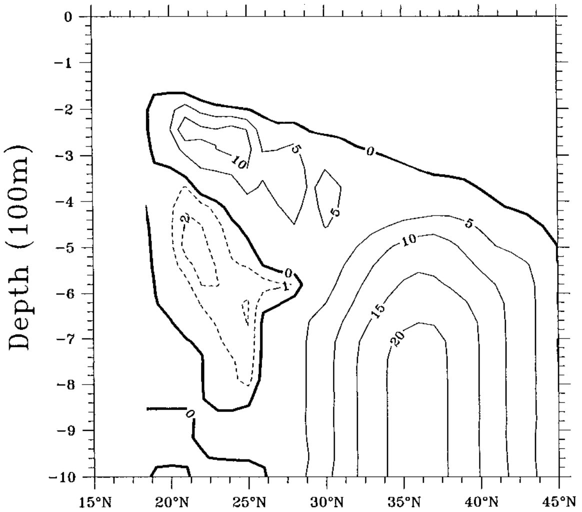

FIG. 19. Isopycnal displacement due to a stronger Ekman pumping rate (in m).

d. Climate variability due to anomalous subpolar mode water formation

We assume that climate variability in the subpolar basin produces an excessive amount of low potential vorticity subpolar mode water. As such anomalous mode water spreads into the subtropical basin, the background stratification changes accordingly. According to the ideal-fluid thermocline theory, potential vorticity in the unventilated thermocline is homogenized toward its value along the intergyre boundary. Thus, weakening of the stratification in the subpolar mode water leads to lowering of potential vorticity for the unventilated thermocline.

To illustrate, we examine the difference between two solutions: a standard solution as described in Fig. 3 and a solution in which the thickness of the unventilated thermocline along the intergyre boundary (or the eastern boundary) is perturbed:

$$\delta h = \Delta h \sin\left(\frac{\sigma - 27.0}{0.8}\pi\right) \quad \text{for } 27.0 \le \sigma \le 27.8. \tag{18}$$

From a simple reduced-gravity model one can infer that weakening of the stratification (smaller reduced gravity) leads to deepening of the wind-driven layer. As shown in Figs. 20, 21, and 22, the continuous stratified model behaves in a similar way. The ventilated layers move downward, and the wind-driven gyre penetrates deeper (Figs. 20c,d). This is consistent with the theoretical analysis presented above; see Eq. (10). On the other hand, the changes in the stratification are primarily confined under the sea surface, with a rather small surface expression. In fact, the maximum difference in the sea surface elevation is no larger than one centimeter.

Changes in the structure of the circulation can be seen

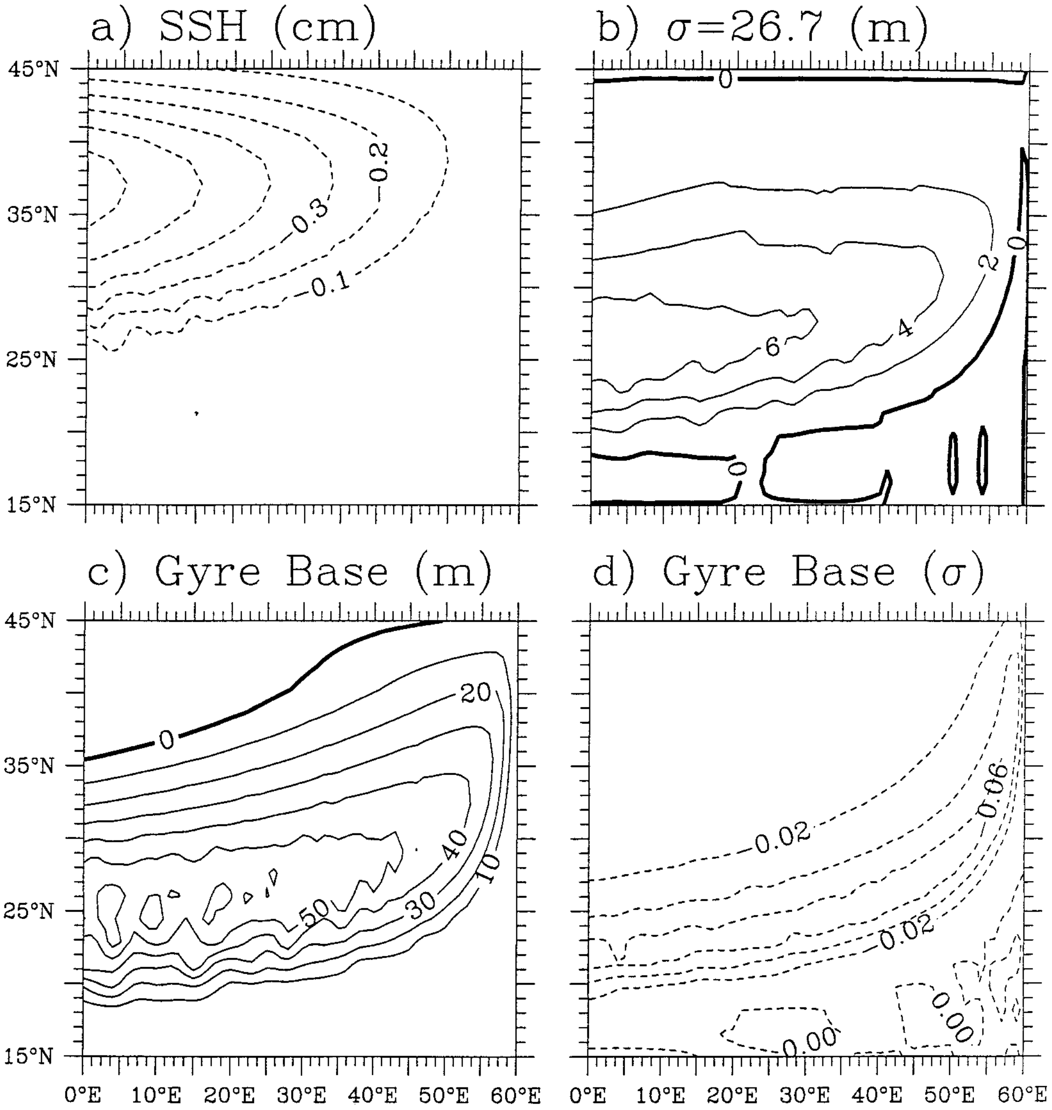

FIG. 20. Changes in the mean fields under a perturbation to the potential vorticity in the unventilated thermocline.

from a meridional section (Figs. 21 and 22). Clearly, the weakening of the stratification in the subpolar mode water leads to a downward movement of both the unventilated and the ventilated thermocline. Joyce et al. (1999) analyzed the historic hydrographic data taken along 50° and 60°W, and showed that over the last two decades isopycnals within the upper 3 km move downward, with a maximum vertical displacement of 100 m at the 2-km level, and gradually decline both upward and downward. Thus, the vertical structure of this type of climate variability diagnosed from the North Atlantic can be interpreted by our ideal-fluid thermocline model.

4. Conclusions

We have examined the climate variability using an ideal-fluid thermocline model with continuous stratification. Although the model is forced by idealized conditions, we believe that climate variability diagnosed from the model may catch the essential structure of the climate variability observed in the oceans. There are several important issues related to the link between this study and other approaches.

First, our model is based on a steady state assumption; that is, climate variability is obtained in terms of the differences between two steady state solutions. As a result, all time-dependent processes are excluded from our study.

Second, the model is based on the ideal-fluid assumption, so dissipation and mixing are set to identically zero in the model. Note that there are still some computational errors accumulating in the downstream direction, as seen in Figs. 17e and 17f. Due to mixing and other processes in the oceans, the lateral spreading

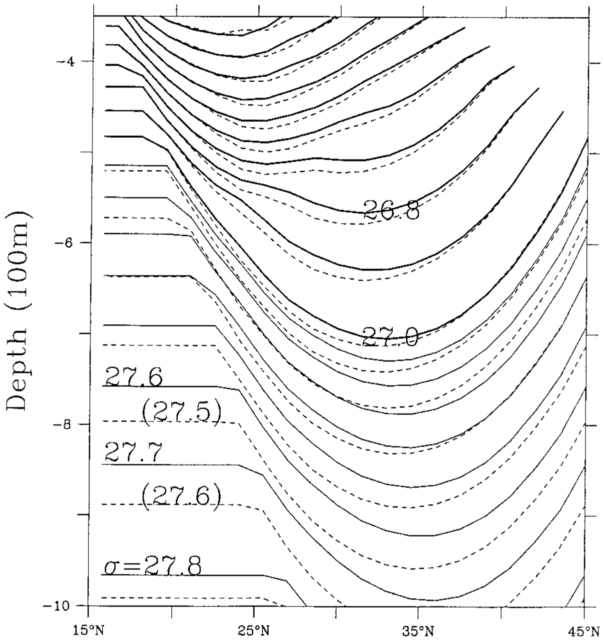

FIG. 21. A density section along 10° off the western boundary of the model basin: solid lines for the standard solution and the dashed lines for the perturbed solution.

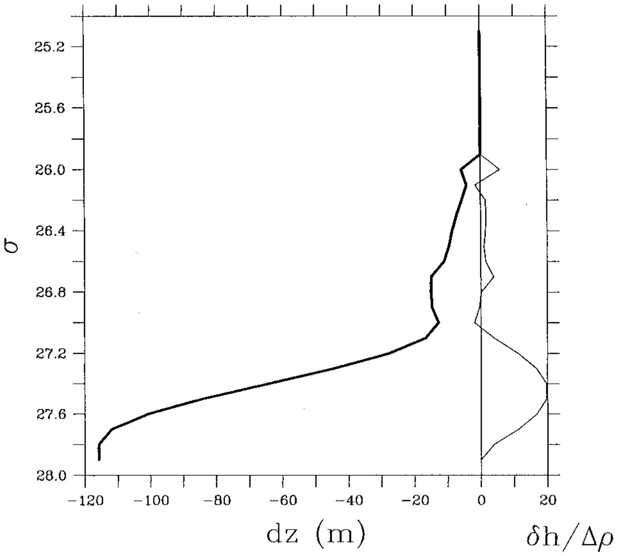

FIG. 22. Depth perturbation at a station (28.5°N, 10°E) in the model basin. The solid line indicates the vertical displacements on each isopycnal, and the thin line indicates thickness perturbation in each isopycnal layer ($\Delta\rho = 0.1\ \sigma$).

of climate anomalies may be more confined to the source area. This is clearly shown in the analyses by Deser et al. (1996), Zhang et al. (1998), and Tourre et al. (1999). However, their studies may also be subject to the quality of the data available. As climate data of high quality accumulates, the climate anomalies diagnosed may have better defined patterns.

Third, our study is focused on climate variability induced by an individual patch of surface anomalous forcing. Climate variability diagnosed from oceanic data, either from a single station or from a basinwide assembled dataset, is a four-dimensional superposition of such anomalies. Thus, in order to understand these observations, we must find out all the small pieces of this big puzzle and put them together into the four-dimensional time–space. Constructing such a dynamical picture for the middle latitude oceans is certainly a major challenge for us. We hope that this study will be a useful step toward this goal.

The major conclusion of this study is that climate variability induced by an anomalous surface forcing propagates downstream, and the perturbations are likely to appear in the form of first and second baroclinic modes. In fact, the first and second modes are the ones most easy to be identified from observations. However, higher modes do exist, although they may be much more difficult to be identified from climate data. It is important to emphasize that the baroclinic modes discussed in this study is different from the traditional baroclinic modes used in wave and stability analysis, although they resemble each other. We have shown intricate wavelike patterns obtained from our numerical model, but these results may contain some numerical artifacts. Nevertheless, we hope these solutions may serve as a straw man for researchers working on climate variability in the ocean. The three-dimensional structure of the perturbations in a truly continuously stratified model of the ideal-fluid thermocline, induced by point source of either thermal forcing or Ekman pumping, remains a challenge.

Acknowledgments. This study was stimulated by conversations with Drs. P. Chang, Z. Liu, R. Lucas, and J. Pedlosky. I was supported by the National Science Foundation through Grant OCE-9616950 to the Woods Hole Oceanographic Institution. Reviwers' critical comments have been a great help in clarifying the ideas and presentation.

APPENDIX

Mathematical Properties of the Thermocline Equations

The ideal-fluid thermocline model satisfies a system of first-order partial differential equations

$$u_x + v_y + w_z = 0, \qquad u\rho_x + v\rho_y + w\rho_z = 0,$$
$$fv_z + \rho_x = 0, \qquad fu_z - \rho_y = 0, \quad \text{(A1)}$$

where ρ stands for $g\rho/\rho_0$. It is convenient to use the matrix notation to derive the characteristics, so we rewrite the equation system in the following form:

$$\mathbf{A}F_x + \mathbf{B}F_y + \mathbf{C}F_z = 0, \qquad \text{(A2)}$$

where

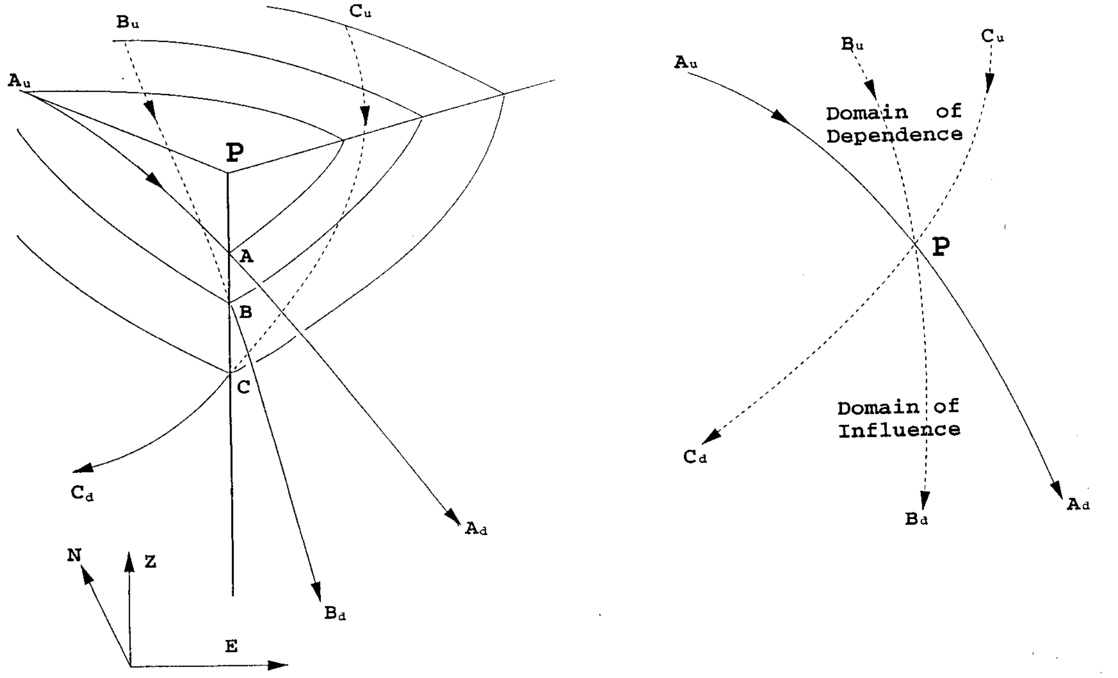

a) Three-dimensional view **b) Two-dimensional view**

FIG. A1. Characteristics the domain of dependence and influence in an ideal-fluid thermocline model: (a) A three-dimensional view depicting the streamlines (characteristics) passing through a single station, and (b) a two-dimensional view of the domains of dependence and influence.

$$\mathbf{A} = \begin{pmatrix} 1 & 0 & 0 & 0 \\ 0 & 0 & 0 & u \\ 0 & 0 & 0 & 0 \\ 0 & 0 & 0 & 1 \end{pmatrix}, \qquad \mathbf{B} = \begin{pmatrix} 0 & 1 & 0 & 0 \\ 0 & 0 & 0 & v \\ 0 & 0 & 0 & 0 \\ 0 & 0 & 0 & -1 \end{pmatrix},$$

$$\mathbf{C} = \begin{pmatrix} 0 & 0 & 1 & 0 \\ 0 & 0 & 0 & w \\ 0 & f & 0 & 0 \\ f & 0 & 0 & 0 \end{pmatrix}, \qquad \mathbf{F} = \begin{pmatrix} u \\ v \\ w \\ \rho \end{pmatrix}. \tag{A3}$$

The characteristic manifold $\Phi(x, y, z) = 0$ of this matrix equation is defined by

$$|\mathbf{A}\Phi_x + \mathbf{B}\Phi_y + \mathbf{C}\Phi_z| = 0, \quad \text{or} \tag{A4}$$

$$f^2\Phi_z^3(u\Phi_x + v\Phi_y + w\Phi_z) = 0. \tag{A5}$$

The first factor, $\Psi_z^3 = 0$, indicates that a vertical line is a triple characteristic. The second factor indicates that a streamline is a simple characteristic. Thus, this system of equations belongs to a high-order hyperbolic system because it has a triple characteristic (Huang 1984).

Since streamlines are simple characteristics of the system, the domain of dependence for a given station is determined by tracing upstream along streamlines passing through this station, such as $\mathbf{A} \rightarrow A_u$, $\mathbf{B} \rightarrow B_u$, and $\mathbf{C} \rightarrow C_u$ in Figs. A1a,b. The domain of influence is determined by tracing downstream along streamlines passing through this station, such as $\mathbf{A} \rightarrow A_d$, $\mathbf{B} \rightarrow B_d$, and $\mathbf{C} \rightarrow C_d$ in Figs. A1a,b.

REFERENCES

Cane, M. A., and E. S. Sarachik, 1976: Forced baroclinic ocean motions. I. The linear equatorial unbounded case. *J. Mar. Res.,* **34,** 629–665.

Deser, C., M. A. Alexander, and M. S. Timlin, 1996: Upper-ocean thermal variability in the North Pacific during 1970–1991, *J. Climate,* **9,** 1840–1855.

Huang, R. X., 1984: The thermocline and current structure in subtropical/subpolar basins. Ph.D. thesis, Massachusetts Institute of Technology and Woods Hole Oceanographic Institution, 218 pp. [WHOI Tech. Rep. WHOI-84-42.]

——, 1988: On boundary value problems of the ideal-fluid thermocline. *J. Phys. Oceanogr.,* **18,** 619–641.

——, 2000: Parameter study of a continuously stratified model of the ideal-fluid thermocline. *J. Phys. Oceanogr.,* **30,** 1372–1388.

——, and S. Russell, 1994: Ventilation of the subtropical North Pacific. *J. Phys. Oceanogr.,* **24,** 2589–2605.

——, and J. Pedlosky, 1999: Climate variability inferred from a layered model of the ventilated thermocline. *J. Phys. Oceanogr.,* **29,** 779–790.

Iselin, C. O'D., 1939: The influence of vertical and lateral turbulence on the characteristics of the waters at mid-depths. *Trans. Amer. Geophys. Union,* **20,** 414–417.

Joyce, T. M., R. S. Pickart, and R. C. Millard, 1999: Long-term hydrographic changes at 52 and 63°W in the North Atlantic subtropical gyre and Caribbean. *Deep-Sea Res. II,* **46,** 245–278.

Liu, Z., 1999: Forced planetary wave response in a thermocline gyre. *J. Phys. Oceanogr.,* **29,** 1036–1055.

McCreary, J. P., 1985: Modeling equatorial ocean circulation. *Annu. Rev. Fluid Mech.,* **17,** 359–409.

Schneider, N., A. J. Miller, M. A. Alexander, and C. Deser, 1999: Subduction of decadal North Pacific temperature anomalies: Observations and dynamics. *J. Phys. Oceanogr.,* **29,** 1056–1070.

Tourre, Y. M., Y. Kushnir, and W. B. White, 1999: Evolution of interdecadal variability in sea level pressure, sea surface temperature, and upper ocean temperature over the Pacific Ocean. *J. Phys. Oceanogr.,* **29,** 1528–1541.

Zhang, R. H., 1998: Decadal variability of temperature at a depth of 400 meters in the North Pacific Ocean. *Geophys. Res. Lett.,* **25,** 1197–1120.

——, L. M. Rothstein, and A. J. Busalacchi, 1998: Origin of upper-ocean warming and El Nino change on decadal scales in the tropical Pacific Ocean. *Nature,* **391,** 879–883.